RESEARCH PAPER

Effect of fabric on shear wave velocity in granular soils

Utkarsh Mital[1] · Reid Kawamoto[1] · José E. Andrade[1]

Abstract

The small-strain elastic shear wave velocity (V_S) is a basic mechanical property of soils and is an important parameter in geotechnical engineering. Recently, V_S has been adopted as one of the indices for development of liquefaction charts. This implies that if a parameter affects V_S, it may also affect liquefaction resistance. Some of the parameters whose effects have been accounted for include relative density, stress state and geologic age. An important parameter that affects both liquefaction resistance and V_S is fabric. Quantification of in situ fabric is still an open problem and hence, considerable judgement is needed in order to map laboratory test results to field conditions. In this paper, we conduct numerical simulations at the grain-scale to investigate the effect of fabric on V_S. We start by showing that two granular assemblies, with the same stress state and void ratio but different fabrics, can exhibit different trends in liquefaction behavior. Furthermore, via a numerical implementation of the bender element test, we obtain two distinct trends of V_S anisotropy for the two granular assemblies. Finally, we consider three different fabric measures based on contact properties and explore correlations between V_S anisotropy and fabric anisotropy. We also look at fabric tensors of the 'strong' and 'weak' network, respectively, of the granular assemblies. Our results suggest that for liquefiable soils, i.e., recent Holocene-age deposits with negligible cementation and with a stress history of seismic loading, a knowledge of V_S anisotropy can give information about fabric anisotropy. A knowledge of in situ fabric could help in more accurately mapping laboratory test results to field conditions.

Keywords Fabric · Liquefaction · Shear wave velocity

1 Introduction

The small-strain elastic shear wave velocity (V_S) is a basic mechanical property of soils and is an important parameter in geotechnical engineering. Together with SPT (standard penetration test) and CPT (cone penetration test) measurements, it helps model the response of geomaterials to dynamic loading processes such as earthquakes and vibrations. Recently, V_S has been adopted as one of the indices for development of liquefaction charts [2, 11, 41]. Liquefaction charts are developed using the "simplified procedure" and are used to evaluate liquefaction resistance of soils in earthquake-prone regions [33].

The use of V_S as an index to quantify liquefaction resistance is based on the fact that both V_S and liquefaction resistance are similarly affected by many of the same parameters (such as void ratio, stress state, stress history and geologic age) [2]. Hence, an understanding of how such parameters affect V_S helps in understanding the effect of such parameters on liquefaction resistance of soils. However, the use of V_S to quantify liquefaction resistance is not without concerns. A major concern arises from the fact that V_S measurements are made at small strains, while liquefaction is a medium- to high-strain phenomenon [2, 41]. It is thought that this discrepancy causes V_S measurements to have a lower sensitivity to factors such as relative density, critical friction angle and dilatancy, when compared to SPT and CPT measurements [11, 21]. The results of this paper help address the aforementioned concern. V_S-based liquefaction assessments are important supplements to the more traditional penetration-based approaches, especially in areas where penetration tests may be unreliable (gravelly soils) or not permitted (landfills). In addition, V_S measurements can be made on small

✉ José E. Andrade
  jandrade@caltech.edu

[1] California Institute of Technology, Pasadena, USA

laboratory specimens, allowing direct comparisons between laboratory and field behavior [2, 41].

An important parameter that affects both liquefaction resistance and V_S is fabric [11]. The term 'fabric' refers to the microstructure of a granular assembly that quantifies the packing of discrete particles and associated voids [10, 15, 42]. Experiments have shown that the method of sample preparation, or the depositional environment, can significantly affect soil fabric and cause soils with the same stress states and relative densities to behave differently [16, 17, 24]. Stokoe et al. [36] proposed empirical correlations relating V_S to confining stresses where the proportionality constant is believed to be a function of soil fabric. More recently, micro-mechanical studies have also been conducted that explore the effect of soil structure or fabric on elastic properties (such as small-strain shear modulus G_{max} or V_S) by means of empirical correlations with stress or void ratio (e.g., [1, 8, 25, 42]). Such studies have proved to be very useful; however, the inherent empiricism in the correlations means that they tend to be soil-specific and have a limited range of application.

The effect of fabric has been established as a major concern when it comes to testing field samples in the laboratory, on account of sampling disturbance destroying the grain fabric. Quantification of in situ fabric is still an open problem and hence, considerable judgement is needed in order to map laboratory test results to field conditions. Given that V_S can be measured both on laboratory specimens and in the field, we are motivated to explore the possibility of quantifying soil fabric using V_S. In this paper, we conduct numerical simulations in two dimensions to investigate the effect of fabric on liquefaction resistance and shear wave velocity (V_S) of soils. We use the 'level set discrete element method' (LS-DEM) [12, 14]—a variant of the discrete element method (DEM) [6] that can accurately depict irregular particle shapes. We conduct our numerical analysis in four steps. First, we generate two granular assemblies that have the same stress state and void ratio but different fabrics. We achieve this by subjecting the two granular assemblies to different stress histories—simple shear and biaxial loading, respectively. Second, we conduct constant-volume biaxial tests and observe that the two assemblies have a different shear strength which manifests in distinct static behaviors. This is expected due to the two assemblies having a different fabric. Third, we conduct a numerical bender element test [18, 27, 35] to determine the trends in V_S anisotropy of the two assemblies. Finally, we consider three different representations of contact fabric to determine whether it is possible to use V_S anisotropy as a proxy for fabric anisotropy.

The novelty of the present study is that it looks at the relationship between fabric and V_S using a more physics-based lens. Our results suggest that a knowledge of fabric anisotropy can give us information about V_S anisotropy, but the reverse—which is arguably more important from an engineering standpoint—may not always be true. For a simple shear stress history, a knowledge of V_S anisotropy could help us in quantifying fabric anisotropy and give us useful insight into the liquefaction resistance of the granular assembly. The same cannot be said for a stress history of biaxial loading. Our micro-mechanical analysis suggests that this discrepancy may be attributed to the differences in behavior of fabric anisotropies for the two stress histories. For the simple shear stress history, the strong and weak fabrics seem to have a similar alignment. This imposes a preferential direction for V_S anisotropy. However, for the biaxially loaded stress history, the strong and weak fabrics seem to have different alignments. The orientation of the weak fabric also contributes to V_S anisotropy since V_S is a small-strain parameter. Hence, for such a sample, knowledge of V_S anisotropy alone is insufficient to uniquely determine fabric anisotropy. This observation is consistent with the well-known concern regarding the use of small-strain V_S to predict liquefaction behavior, which is a medium- to large-strain phenomenon [2, 11, 41] and being a measure of deviatoric strength, maybe considered to depend on the strong fabric [29].

We close by suggesting that for recent (Holocene-age) deposits with negligible cementation and with a seismic history, V_S anisotropy could provide useful information about fabric anisotropy and consequently liquefaction resistance. From a practical viewpoint, the constraints placed on the soils are not a big concern since liquefaction assessments are generally done on liquefiable soils—soils that meet the aforementioned constraints, thus also supporting the prevalent practice of using V_S-based liquefaction charts. A knowledge of in situ fabric obtained via V_S measurements could enable development of more physical procedures to map laboratory or simulation results to field conditions.

2 Simulation methodology

We conduct our numerical investigation using the 'level set discrete element method' (LS-DEM) [12, 14]. LS-DEM is a variant of the discrete element method (DEM), which is a numerical method that describes the mechanics of an assembly of particles [6]. LS-DEM enables an accurate depiction of irregular particle shapes using level sets. In this work, we use a 2D level set representation of caicos ooid grains as obtained by Lim et al. [20], following the characterization methodology proposed by Vlahinic et al [39]. These grains are fairly well rounded, with aspect ratios ranging between 1 and 2. They are obtained in dimensions of pixels, which we rescale assuming a pixel

size of 0.1095^2 mm^2, yielding a mean grain area of 5.4 mm^2. Thickness of grains is assumed to be 1 pixel length. Table 1 outlines the values of model parameters used in the LS-DEM model. The same model parameters were used for both static (i.e., biaxial) and dynamic (i.e., bender element) simulations. Our damping model involved the use of a high value of global damping (5×10^3 s^{-1}), coupled with zero contact damping. The simple approach of using only global damping was checked by conducting a verification exercise, as reported in Appendix. Our time step is equal to 1.36 µs, which is smaller than the critical time step required for stable DEM analysis [37]. To determine the value, we followed the approach of Tu and Andrade [37] using the critical time step corresponding to conventional circular-grain DEM as a starting point. The particle with the smallest area was considered, and the radius of an equivalent circle was used to calculate the critical time step for a system with rotational degrees of freedom. Since the grain shapes in the present work are more complicated, we used a time step smaller than the calculated value as an extra precaution.

2.1 Initial fabric quantification

We initially quantify fabric using the classic second-order tensor based on contact normals [13], hereafter referred to as the contact tensor:

$$F_{ij} = \frac{1}{N} \sum_{c=1}^{N} n_i^c n_j^c \qquad (1)$$

where n_i^c is the i−th component of contact normal at contact c. The fabric anisotropy A is defined as:

$$A = 2(F_1 - F_2) \qquad (2)$$

where F_1 and F_2 are the major and minor principal values, respectively, of the contact tensor. The orientation (θ_1) of F_1 may be used to define the orientation of contact

anisotropy A. We can use a second-order Fourier expansion to obtain the orientational distribution $P(\theta)$ of contact normals [4]:
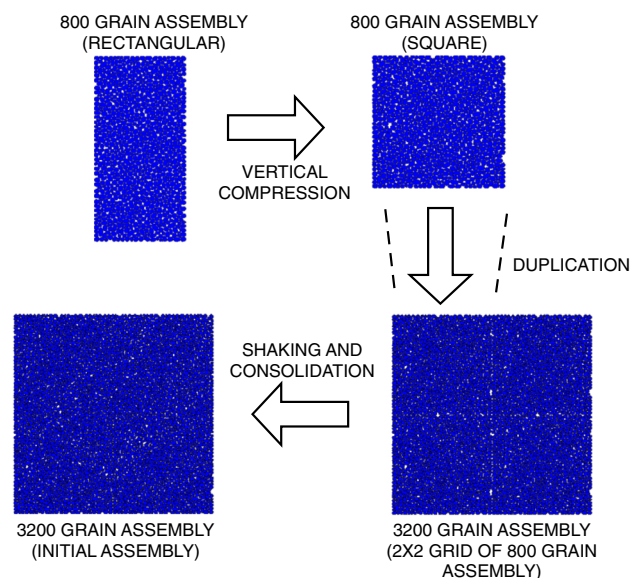
$$P(\theta) = \frac{1}{2\pi} \{1 + A \cos 2(\theta - \theta_1)\} \qquad (3)$$

where θ is the orientation of a contact normal. A perfectly isotropic fabric will be circular in polar coordinates, whereas an anisotropic fabric will tend toward a 'peanut' shape.

This gives us an initial understanding for the fabric of our granular assemblies. There are many different ways to quantify fabric [3, 15]. In Sect 5, we will discuss other fabric representations.

2.2 Granular assembly generation

Our objective in this section is to obtain two granular assemblies with respective stress histories of simple shear and biaxial loading, such that they have similar stress states and void ratio but different fabrics. Figure 1 summarizes our methodology to obtain an initial assembly. The initial assembly needs to be dense. This is because the numerical analysis of the bender element test was based on the works of O'Donovan et al. [28] where the numerical DEM assemblies were dense. The need for dense assemblies implies more computational effort, which is all the more significant since we estimate that in 2D, LS-DEM simulations cost an order of magnitude more time compared to conventional DEM. Hence, we pursue an unconventional approach to assembly generation. We initially generate a hexagonal packing of 800 grains in an approximate aspect ratio of 1:2. The assembly is isotropically consolidated to 5

Table 1 Model parameters and values used in the LS-DEM model

| Model parameters	Values
Inter-particle friction	0.3
Wall friction	0
Normal contact stiffness (particle and wall)	2.74×10^8 N/m
Particle shear contact stiffness	2.47×10^8 N/m
Particle density	2.7×10^3 kg/m^3
Global damping	5×10^3 s^{-1}
Contact damping	0
Time step	1.36×10^{-6} s

Fig. 1 Initial assembly generation

MPa and unloaded to 100 kPa, and then the horizontal and vertical boundaries are moved to change the aspect ratio to 1:1. The assembly is then allowed to relax with the inter-particle friction turned off to result in a dense stress-free assembly. However, a larger assembly is desired to obtain estimates of V_s in different directions, as described in Sect. 4.2. Therefore, we duplicate the 800-grain assembly in a 2×2 grid, which results in clear interfaces at the boundaries of the individual 800-grain assemblies. To remove the interfaces, we shake the 3200 grain assembly. The assembly is then allowed to relax with the inter-particle friction turned off, resulting in a stress-free assembly. Finally, we turn the inter-particle friction back on and isotropically consolidate the assembly to 100 kPa. This serves as our initial granular assembly.

Our initial granular assembly has a high inherent contact anisotropy (Fig. 2a) and an isotropic stress state (Fig. 3a). We subject this assembly to two different loading histories—simple shear and biaxial loading, respectively—with the constraint that the two resultant assemblies should have similar stress states and void ratio. This constraint helps isolate the effect of fabric. We refer to the two assemblies as 'assembly 1' and 'assembly 2'. The loading history for assembly 1 involves half a cycle of simple shear loading, wherein the assembly is sheared to an angle of 20°, and subsequently sheared back to 0°. This significantly alters the initial contact anisotropy, giving the assembly a pronounced diagonal anisotropy (Fig. 2b), with the principal direction of the contact tensor at an angle of 34° clockwise with the vertical. Furthermore, this loading history results in the assembly having a residual deviatoric stress, owing to the inherent non-elastic nature of the system. The assembly has a resultant void ratio of $e = 0.17$, and a stress

state of $p = 85$ kPa, and $q = 30$ kPa. Here, $p = (\sigma_{11} + \sigma_{22})/2$ is the mean stress (or pressure), and $q = \sqrt{(\sigma_{22} - \sigma_{11})^2 + 2\sigma_{12}^2}$ is the deviatoric stress. σ_{11} is the horizontal stress, σ_{22} is the vertical stress, and σ_{12} is the shear stress. Note that the drop in mean stress to 85 kPa is on account of subjecting the assembly to a stage of relaxation (after simple shear loading) to allow any vibrations to damp out and to let the assembly reach static equilibrium. A visualization of the anisotropic stress state of assembly 1 (Fig. 3b) shows how the stress-induced anisotropy affects the contact fabric (Fig. 2b).

The loading history for assembly 2 involves biaxial loading, with the constraint that the final stress state and void ratio should be similar to that of assembly 1. We first subject assembly 2 to isotropic unloading, and subsequently to vertical compression at constant horizontal stress, resulting in the same p and q as assembly 1. The contact anisotropy of the second assembly is predominantly vertical, oriented at an angle of 5° counter-clockwise with the vertical (Fig. 2b). This is very similar to the inherent contact anisotropy in the initial assembly, which is oriented at an angle of 7° counter-clockwise with the vertical (Fig. 2a). Assembly 2 has a resultant void ratio of $e = 0.15$. The void ratios of the two assemblies are similar but not exactly the same and may have a small contribution towards different macroscopic behaviors of the two assemblies. However, it will become apparent in Sects. 3 and 5 that the different macroscopic behaviors of the two assemblies can be attributed to them having a different fabric.
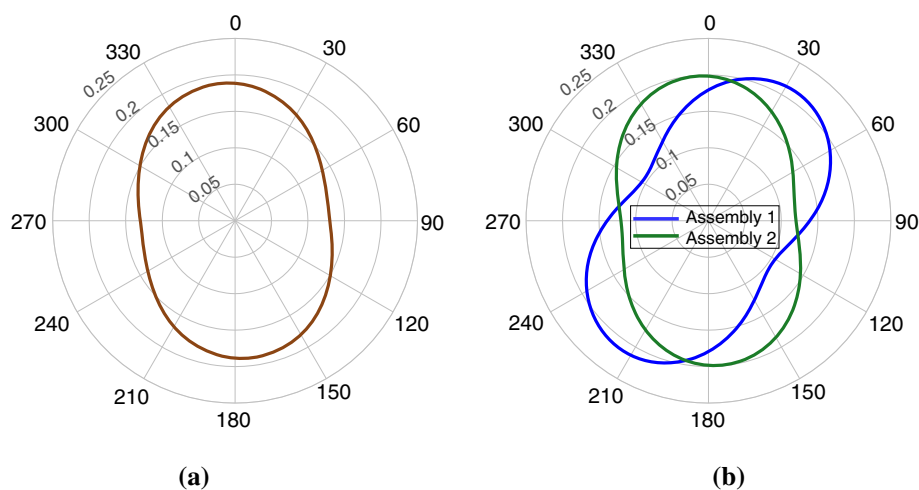
Fig. 2 Contact anisotropies of different assemblies—the rose diagrams show the orientational distribution of contact normals (clockwise from vertical, in degrees). **a** Initial assembly with $A = 0.19$, $\theta_1 = -7$ °. **b** Assembly 1 with $A = 0.34$, $\theta_1 = 34$ °, Assembly 2 with $A = 0.25$, $\theta_1 = -5$ °. Here A is contact anisotropy and θ_1 is the orientation of the maximum principal value measured clockwise from the vertical, as defined in Sect. 2.1
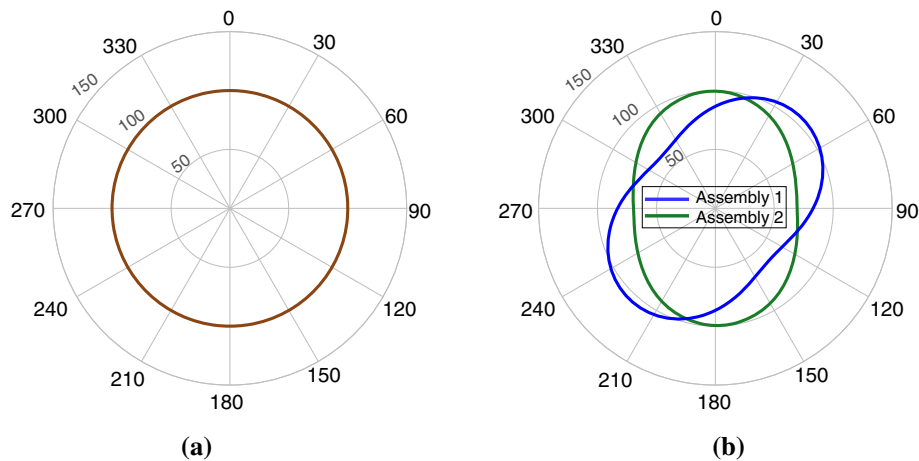
Fig. 3 Stress anisotropies of different assemblies. **a** Initial assembly with an isotropic stress state, $p = 100$ kPa, $q = 0$ kPa. **b** Assembly 1 and Assembly 2, both with $p = 85$ kPa, and $q = 30$ kPa

Remark 1 Since we have subjected assembly 1 to half a cycle of simple shear loading, conceptually it may be considered as being subjected to forces similar to those imposed on soil elements during an earthquake. This follows Seed and Peacock [34], where it has been discussed that the main forces acting on in situ soil elements during an earthquake are due to an upward propagation of shear waves. These waves impose reversible shear stresses on the soil element. Furthermore, it has been discussed that an irregular stress history during an earthquake may be considered equivalent to a number of uniform loading cycles, for the purposes of determining liquefaction resistance [32, 33]. Hence, assembly 1 may be considered to be analogous to a recent soil deposit with seismic history; this may be considered "liquefiable" for the purposes of liquefaction strength assessment, as discussed in the introduction. Note that we mean 'recent' to imply soil deposits where aging effects due to cementation are negligible (which is true for Holocene-age deposits). On the other hand, assembly 2 may be considered to be analogous to a recent soil deposit with no seismic history.

3 Static behavior

Liquefaction behavior is associated with undrained loading of saturated granular soils. A common approach to modeling such behavior involves assuming that the bulk modulus of pore water is large with respect to the bulk modulus of the soil skeleton. As a result, undrained loading of a saturated soil can be simulated by imposing a constraint of constant-volume on a dry assembly. In this section, we consider the static behavior of the two assemblies under two cases of biaxial loading, both under the constraint of constant-volume. In the first case, both the assemblies are

compressed in the vertical direction. Results are shown in Fig. 4a, b. Assembly 2, whose contact fabric anisotropy is largely aligned with the direction of vertical compression, shows stable strain-hardening behavior. However, assembly 1, whose contact fabric anisotropy is oriented at an angle of 34° to the vertical, shows extensive strain-softening associated with liquefaction behavior. In the second case, both the assemblies are compressed in the horizontal direction (Fig. 4c, d). Assembly 1 exhibits a behavior very similar to the vertical compression case. Assembly 2, however, behaves very differently under horizontal compression. It starts by strain-softening spontaneously, almost going through what may be considered an 'unloading' phase and reaches an almost isotropic stress state. Subsequently, it undergoes a phase of rebuilding and then liquefies again, exhibiting the classic hook pattern. Note that in field assessments of liquefaction resistance, it is behavior under vertical compression that is relevant, and hence assembly 1 may be considered to be liquefiable. Horizontal compression was considered here for the purposes of exploring the difference in behavior of the two assemblies.

Given the respective fabric anisotropies of the two assemblies (Fig. 2 and insets of Fig. 4b, d), this difference in static behavior is expected. It is well known that a high contact anisotropy in the direction of loading facilitates load transmission through the granular assembly [19, 30]. Assembly 1 has contacts largely oriented away from both the horizontal and vertical, and hence has a low deviatoric strength under both vertical and horizontal compression. Assembly 2 has contacts largely oriented along the vertical, hence it has a high deviatoric strength along the vertical direction and has almost no strength along the horizontal direction. This results in an immediate catastrophic failure (more pronounced than assembly 1) when subjected to horizontal compression. Presumably, during this process,
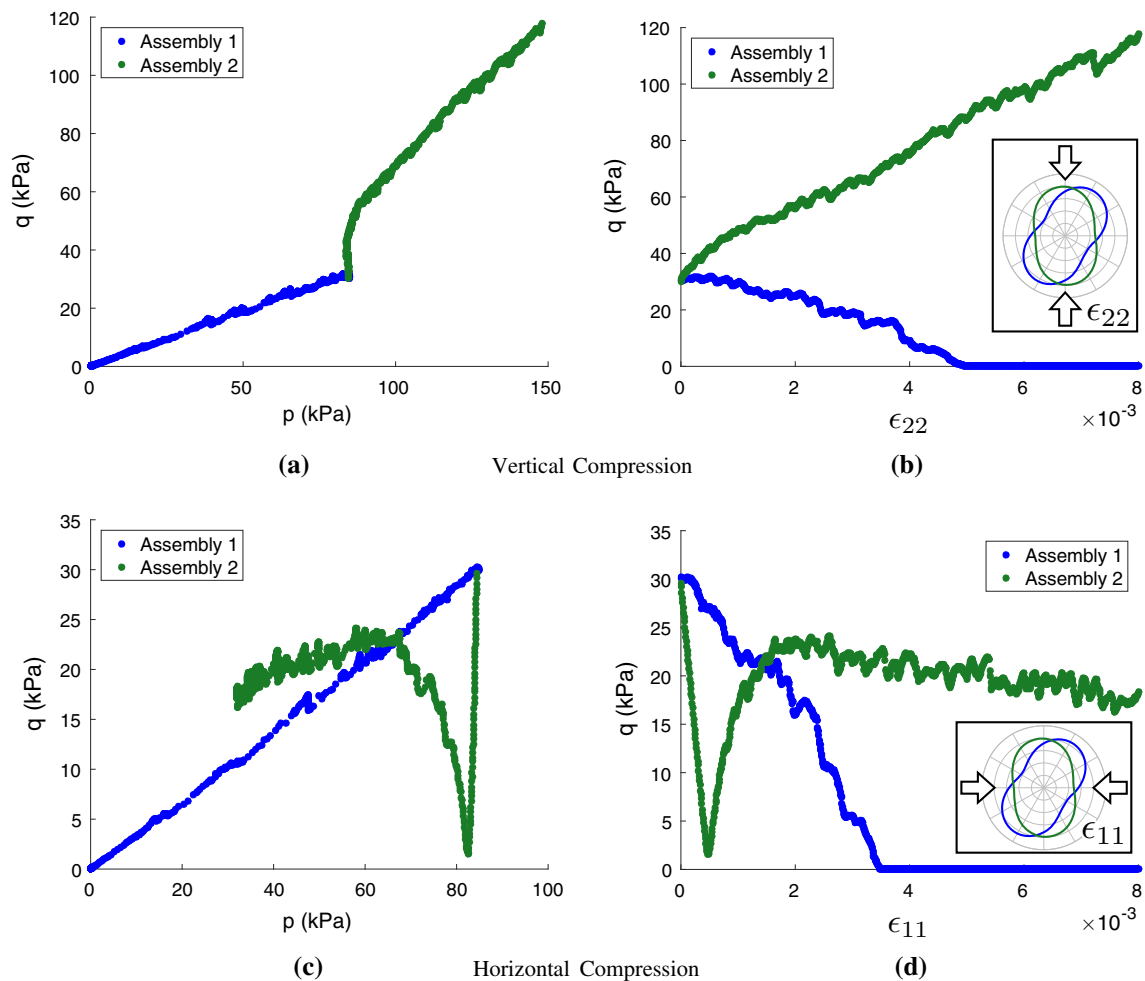
Fig. 4 Static behavior of the two granular assemblies under constant-volume compression. **a**, **b** show results for constant-volume vertical compression; **c**, **d** show results for constant-volume horizontal compression. **a**, **c** deviatoric stress (q) versus volumetric stress (p). **b** Deviatoric stress (q) versus vertical strain (ϵ_{22}). **d** Deviatoric stress (q) versus horizontal strain (ϵ_{11}). Insets in (**b**) and (**d**) show direction of compression in relation to the initial fabric

the contacts re-align giving the assembly some strength to support deviatoric loads in the horizontal direction, before liquefying again. In this work, our focus is on the initial state of the assemblies, prior to biaxial loading, so we do not delve into what the intermediate state of the assemblies may look like. The evolution of contact anisotropy during such intermediate states is a subject of considerable interest in the literature [9, 43]. Importantly, Fig. 4 clearly demonstrates how two granular assemblies with the same stress state and similar void ratio can exhibit different behavior if their fabric is different.

4 Shear velocity tests

Having seen the two assemblies show distinct liquefaction behaviors, we now seek to estimate the small-strain shear velocities of the two assemblies. From the prevalent

understanding of V_S-based liquefaction correlations, we expect assembly 2 to have a higher vertical V_S than assembly 1. For horizontal V_S, however, we might expect assembly 1 to do better than assembly 2. However, the results of this section are not as expected, thus bringing into light a need to exhibit care while using V_S to estimate liquefaction resistance. We will discuss that further in Sect. 5.

4.1 Numerical bender element test

We estimate the shear wave velocity (V_S) by simulating a 'bender element test' [18, 27, 35]. The bender element test is a common experimental test to measure shear wave velocity in soils. It consists of a transmitter element that generates a shear wave, and a receiver element that detects the transmitted disturbance. We choose a bin of particles as the transmitter element and implement rigid walls at the

boundaries of the assembly. In simulations, as opposed to experiments, it is possible to know the displacement of each particle. Hence, instead of having a single particle act as a receiver, we track the shear displacement for a central column of grains (away from the boundaries) along the entire length of the assembly (denoted by grains colored with a black to white gradient in Fig. 5). This simplifies the analysis as it becomes convenient to identify shear waves. The assembly is discretized into bins with approximate dimensions of 40×40 pixels, or 4.4×4.4 mm^2. We plot two-dimensional contours of the central column of particle displacements along the direction of propagation. In the contour plot, the zero crossings of the received signals are clearly visible as a distinct contour line. The average slope of this line is then taken as the shear wave velocity [28]. Figure 6 shows the bender element test results for an 800 grain assembly, isotropically consolidated to 50 kPa. The transmitter bin is the bottom-most bin of the central column. The slope of the zero contour line yields a shear velocity estimate of $V_S \approx 200$ m/s.

A common input signal is a single sine wave. For a clear output response, it is desirable for the frequency of the sine wave to approach the resonant frequency of the system. Since we need to estimate V_S in different directions, we need to know the resonant frequency in each direction since it is affected by soil stiffness [18]. To circumvent this issue, we use a square wave input with a rise time of 100 time steps and amplitude of 1 pixel length. A square wave is a robust input signal that contains all the frequencies and generates a clear response regardless of soil stiffness [18]. A drawback of the square wave is that the system response necessarily exhibits a 'near-field' effect due to faster

moving compressional waves [31]. As a result, it is often not straightforward to determine the arrival of the shear wave. Although the point of first inflection is sometimes considered to be a fair estimate of shear wave arrival [38], research suggests that the arrival of the shear wave does not correspond to a distinctive point in the signal [23]. Various signal interpretation techniques exist to aid in estimating shear wave velocity in an experimental bender element test [28, 40]. For our purpose, since we have access to displacement of each particle, we track the shear displacement for a central column of grains along the entire length of the assembly. Note that the area on the contour plot between the initial noise and the zero contour line corresponds to the near-field effect [28].

Remark 2 For a verification of our implementation of the bender element test, refer to Appendix. The verification exercise involves obtaining a true value of V_S—via a static biaxial test—of the assembly shown in Figure 5. The value of V_S obtained in Fig. 6 is checked against the aforementioned true V_S. The true V_S is also used as a basis for determining the appropriate discretization of the assembly into bins—as mentioned earlier in the section. It is also used as a basis for checking the appropriateness of our damping model, as well as for checking the amplitude of the input square wave. Amplitudes larger than 1 pixel length (0.1095 mm) resulted in plastic deformations and the shear velocity obtained did not correspond to small-strain or elastic stiffness.

4.2 Shear velocity results

We use the numerical bender element test technique described in Sect. 4.1 to obtain V_S estimates for the two 3200-grain assemblies. We estimate V_S in different directions to investigate the correlation of anisotropy of V_S with the fabric. Recall from Sect. 2.2 that both assembly 1 and assembly 2 have similar macroscopic stress states ($p = 85$ kPa, $q = 30$ kPa) and void ratios ($e = 0.17$ and 0.15, respectively).

We start by estimating V_S in the vertical direction. Figure 7 shows sample contour plots with slope estimates, for the 3200-grain assembly 1 and 3200-grain assembly 2. For these plots, the transmitter bin is not always the bottom-most bin of the central column. Different locations of the transmitter bin along the central column yield slightly different V_S estimates, owing to the inherent heterogeneity of the assembly. It is also possible that our technique of assembly generation induced further heterogeneities in the grain fabric. Hence, multiple tests (at least three) are simulated with transmitter bins placed at different locations along the central column in order to obtain statistical estimates of V_S. For certain tests, contour plots do not yield
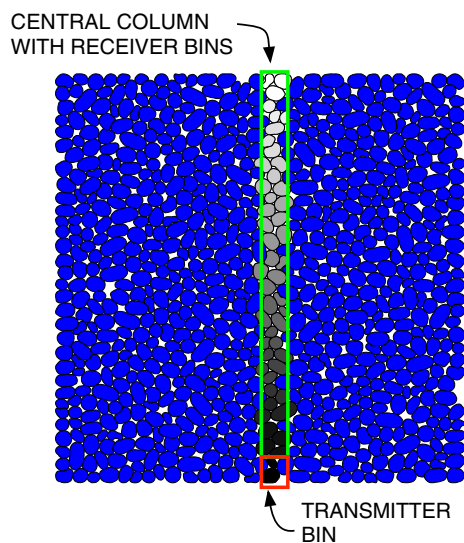
Fig. 5 Illustration of how shear displacement is tracked for a central column of grains. The central column is denoted by grains that are colored with a black to white gradient
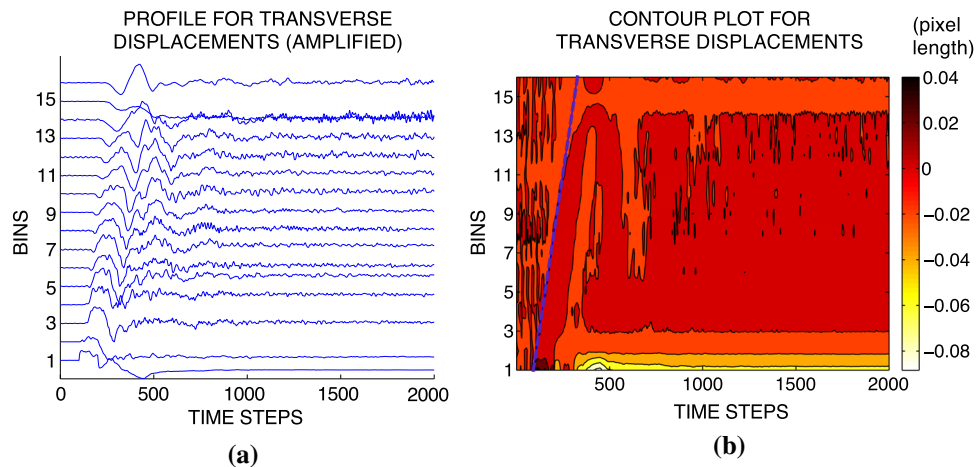
Fig. 6 Shear velocity estimate for the assembly in Fig. 5. The blue line in the contour plot in (**b**) is the average slope estimate for the zero crossing of the received signal. 1 bin = 40 × 40 pixels, 1 pixel length = 0.1095 mm, 1 time step = 1.36 μs
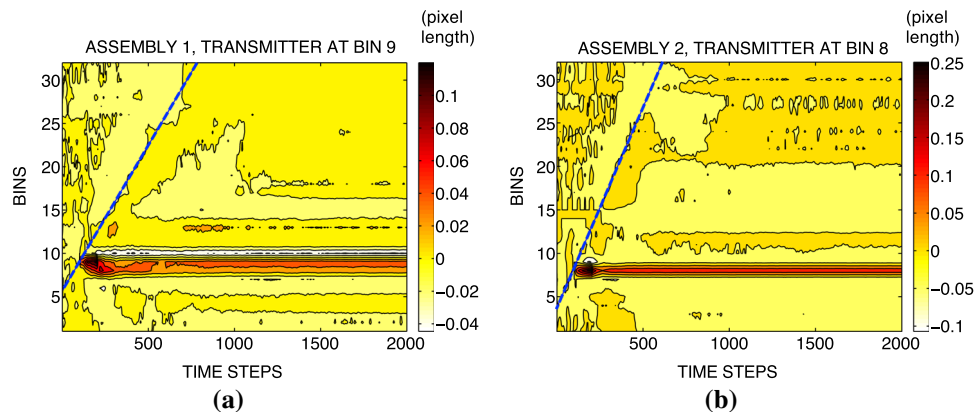

Fig. 7 Example contour plots for transverse displacement. **a** assembly 1. **b** assembly 2. The dashed blue line on the plots is the average slope estimate for the zero crossing of the received signal, which yields a V_S estimate (110 m/s for assembly 1 and 148 m/s for assembly 2). 1 bin = 40× 40 pixels, 1 pixel length = 0.1095 mm, 1 time step = 1.36μs. Note that the assembly 1 example showing a more distinctive crossing than the assembly 2 example has no special meaning and can be attributed to the inherent heterogeneity of the assemblies

distinct contour lines corresponding to zero crossing. Figure 8 shows one such test, where there is a high signal dissipation resulting in the lack of a distinct contour line beyond the first few receiver bins. A distinct contour line is necessary in order to estimate its average slope, and consequently V_S. While estimating the slope, we consider a subset of the contour line to ensure that the average slope line (dashed blue line in Figs. 6 and 7) passes the transmitter bin near the time step corresponding to initiation of the input wave. Following this approach, the mean vertical V_S for assembly 1 was estimated to be 110 m/s, while for assembly 2 it was estimated to be 131 m/s. A preliminary justification for these values can be obtained from Fig 2b. Assembly 2 has contacts largely oriented along the vertical—facilitating faster load transmission in the vertical direction resulting in a higher vertical V_S. This is not the case for assembly 1. This is also consistent with the respective behavior of the two assemblies under constant-

volume vertical compression (Fig. 4a, b), as discussed in Sect. 3.

In order to investigate correlations between V_S anisotropy and fabric anisotropy (Sect. 5), we need to obtain estimates of V_S in different directions for both the assemblies. We conduct an 'angle sweep', i.e., we conduct tests where the transmitter bin is sheared at an angle to the horizontal to transmit a shear wave at an angle. Figure 9 illustrates one such test configuration. The central column (denoted by grains with a black to white gradient) which acts as the receiver is inclined, or rotated, at the same angle with the vertical. Furthermore, the transmitter bin is placed away from the boundaries to prevent wave reflections from corrupting the test results. Different locations of the transmitter bin along the central column yield slightly different V_S estimates, owing to the inherent heterogeneity of the assembly. Hence, multiple tests (at least three) are simulated with the transmitter bin placed at different
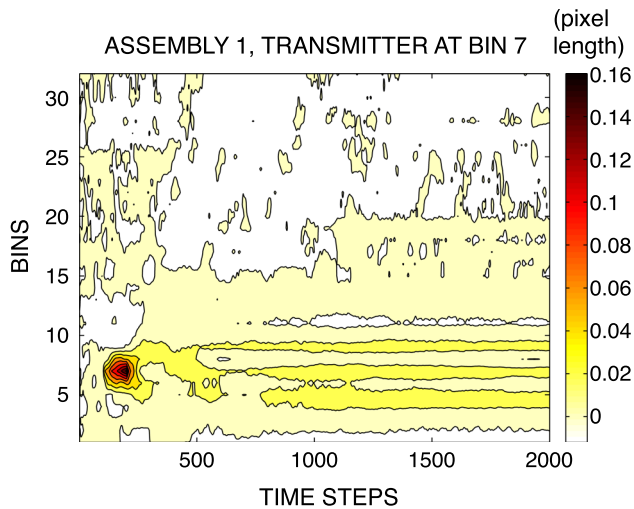
Fig. 8 Contour plot for transverse displacement, for assembly 1 with transmitter at bin 7. Note the high signal dissipation and the lack of a distinct contour line beyond the first few receiver bins, which disables a V_S estimation. 1 bin = 40 × 40 pixels, 1 pixel length = 0.1095 mm, 1 time step = 1.36μs
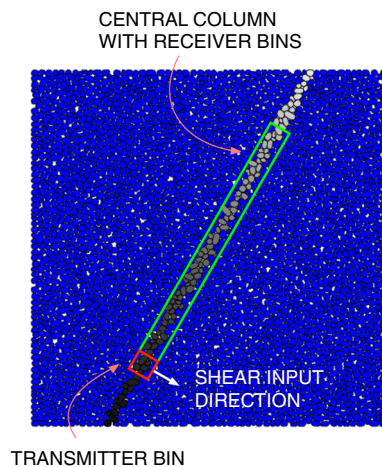
Fig. 9 Illustration of how V_S estimates are obtained in different directions. The central column (denoted by grains that are colored with a black to white gradient) is rotated at a desired angle with the vertical. The transmitter bin is located in the central column and is sheared perpendicular to the inclination of the central column. Compare with Fig. 5

locations along the central column to obtain statistical estimates of V_S. As with the vertical V_S tests, not all tests yield contour plots with distinct contour lines corresponding to zero crossing. For the 'angle sweep', the inclination angle θ of the central column is varied from $(-90, 90]°$, in increments of 30°. The angle is positive when measured clockwise from the vertical. This yields V_S estimates for the entire rotation of 360° since the central column is the same for rotation of θ and $\theta + 90$ (°). Figure 10 shows the results of the 'angle sweep' for assemblies 1 and 2. Assembly 1 has a pronounced V_S anisotropy, with a

markedly high V_S at an angle of 30°, clockwise with the vertical. Assembly 2 also shows some anisotropic behavior, although less so compared to assembly 1. Interestingly, assembly 2 has a high V_S in the horizontal direction, suggesting a high liquefaction resistance when compressed horizontally. However, this is inconsistent with the results in Fig. 4c, d. We will discuss some of the possible micromechanics responsible for this discrepancy after quantifying the fabric in the next section.

5 Quantification of fabric

In Sect. 2.1, we did an initial quantification of the granular fabric using contact normals. We now consider a few more fabric measures and gauge their correlations with V_S anisotropy. V_S is considered to be a measure of shear stiffness of a granular assembly, since it is related to the small-strain elastic shear modulus via the wave equation. From a micromechanical perspective, since force transmission takes place through contacts between the grains, fabric measures based on contact properties are considered to be closely related to the stiffness response of a granular assembly, as opposed to particle-based fabric measures [15]. Therefore, we focus our investigation on fabric measures based on contact properties.

Specifically, we consider three fabric tensors. These are (1) contact tensor (same as Sect. 2.1), (2) branch tensor (based on branch vectors), and (3) mixed tensor (based on a mix of contact normals and branch vectors). In addition, we also consider fabric tensors defined using subsets of all contacts, namely the 'strong' and 'weak' contacts [29]. 'Strong' contacts refer to contacts carrying forces greater than the mean contact force. On the other hand, 'weak' contacts refer to contacts carrying forces lower than the mean contact force. Strong contacts tend to be aligned with the maximum principal stress and carry most of the deviatoric loads imposed on an assembly. The alignment of weak contacts, however, tends to depend on stress history. Under biaxial loading, weak contacts tend to be aligned perpendicular to the strong contacts and ostensibly help in propping them up [29]. Contrarily, under conditions of simple shear, it has been shown that weak contacts have the same alignment as strong contacts and ostensibly help in carrying deviatoric load [7]. We will observe this history-dependence of weak contacts in the next three Sects. (5.1–5.3), which will inform our discussion regarding correlations of fabric with V_S in Sect. 5.4. The results of sections 5.1–5.3 will also help us discuss the oft-quoted criticism against the use of V_S for assessing liquefaction susceptibility of soils—that V_S is a small-strain elastic parameter while liquefaction is a medium-to-large-strain plastic phenomenon.
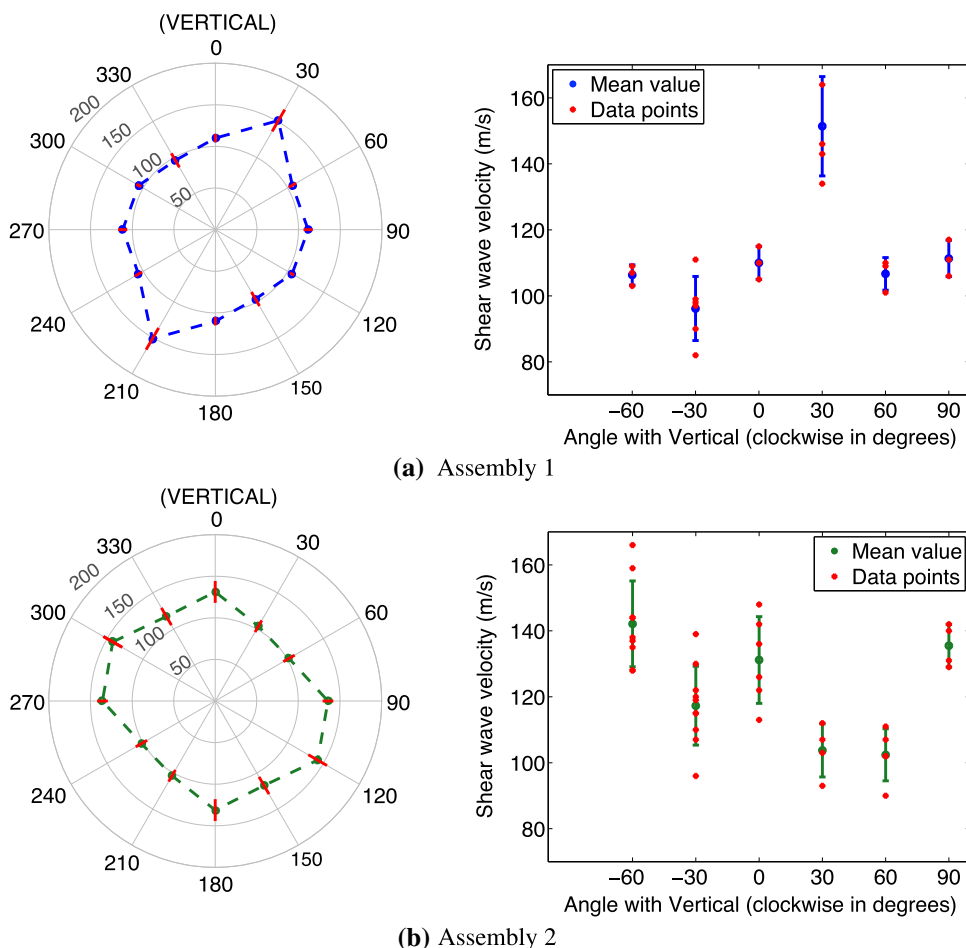
Fig. 10 Results of V_S 'angle sweep', giving estimates of V_S in different directions. **a** Assembly 1, **b** Assembly 2. Left: Polar plot with the radius corresponding to V_S in m/s, and angle corresponding to angle with vertical (clockwise in degrees). Right: Linear plot of V_S or shear wave velocity, in m/s versus angle with vertical (clockwise in degrees). The error bars correspond to one standard deviation

5.1 Contact tensor

The contact tensor is a fabric tensor based on contact normals, as defined in Sect. 2.1. It was one of the first fabric measures proposed to study stress-induced anisotropy in granular assemblies [13]. This definition was motivated by the fact that the macroscopic stress is transmitted microscopically via contact forces in a granular assembly. In addition to the fabric quantification in Eq. 1, we consider the 'strong' and 'weak' subsets of contacts in the assembly to define two more fabric tensors:

$$F_{ij}^S = \frac{1}{|S|} \sum_{c \in S} n_i^c n_j^c \qquad (4)$$

$$F_{ij}^W = \frac{1}{|W|} \sum_{c \in W} n_i^c n_j^c \qquad (5)$$

where S refers to the set of strong contacts and W refers to the set of weak contacts, respectively, in a granular assembly. $|S|$ and $|W|$ are the cardinality of S and W,

respectively, which refers to the number of elements in each set. The anisotropy of the fabric tensors in Eqs. 4 and 5 is defined in the same manner as in Eq. 2. The orientational distribution of the contact normals in the strong and weak subsets is defined using the second-order Fourier expansion as shown in Eq. 3. Figure 11 shows the orientational distribution of the contact tensor for (a) all contact normals, (b) strong contact normals, and (c) weak contact normals.

5.2 Branch tensor

The branch tensor is a fabric tensor based on branch vectors and was proposed by Magoariec et al. [22] as a possible internal variable to account for the structural or inherent anisotropy of a granular assembly. It is defined as:

$$G_{ij} = \frac{1}{N} \sum_{c=1}^{N} l_i^c l_j^c \qquad (6)$$
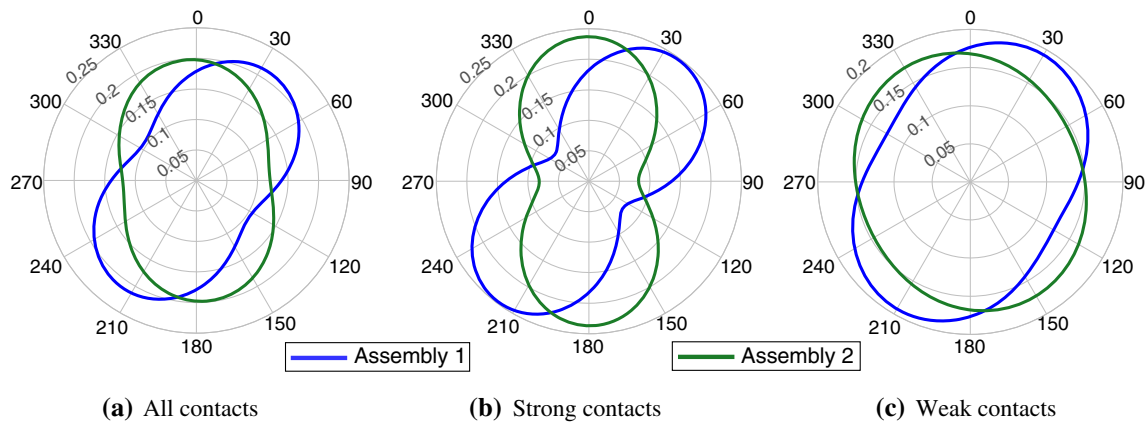
Fig. 11 Orientational distribution of contact tensor. The directions are clockwise from vertical (in degrees). **a** Assembly 1: $A = 0.34$, $\theta_1 = 34°$; Assembly 2: $A = 0.25$, $\theta_1 = -5$ °. **b** Assembly 1: $A = 0.55$, $\theta_1 = 37$ °; Assembly 2: $A = 0.49$, $\theta_1 = -1°$. **c** Assembly 1: $A = 0.21$, $\theta_1 = 29°$; Assembly 2: $A = 0.09$, $\theta_1 = -25°$

where l_i^c is the i-th component of the branch vector as contact c, and N is the number of contacts in the granular assembly. The anisotropy of the branch tensor is defined as:

$$A = \frac{2(G_1 - G_2)}{\mathrm{tr}(\boldsymbol{G})} \tag{7}$$

where G_1 and G_2 are the major and minor principal values, respectively, the boldface $\boldsymbol{G}$ refers to the branch tensor, and $\mathrm{tr}(\boldsymbol{G}) = (G_1 + G_2)$ refers to the trace of $\boldsymbol{G}$. Note that for ease of presentation, we use A to define anisotropy for all types of fabric tensors considered in this work, where the specific fabric tensor in question is clear from the context. The orientational distribution of the branch tensor is calculated in a manner similar to Eq. 3. The relationship in Eq. 3 assumes that the trace of the fabric tensor is 1, which is why we normalize the anisotropy of the branch tensor by the trace. Furthermore, we also define branch tensors for the strong and weak contacts of the granular assembly, in a manner similar to Eqs. 4, 5.

The definition of branch tensor was motivated by numerical tests on granular assemblies of non-spherical particles where it was observed that the contact tensor was unable to sufficiently predict the macroscopic stresses [26]. The branch tensor captures the relative positions of particles, which are relevant for quantifying the macroscopic stress state [5]. It also helps capture the effect of shape in non-spherical assemblies since contact normals and branch vectors are not collinear. Figure 12 shows the orientational distribution of branch tensor for (a) all contacts, (b) strong contacts, and (c) weak contacts.

5.3 Mixed tensor

The mixed tensor is a fabric tensor based on both contact normals and branch vectors and was proposed by Kuhn et al. [15]. It may be defined as:

$$H_{ij} = \frac{1}{N} \sum_{c=1}^{N} l_i^c n_j^c \tag{8}$$

The anisotropy of the mixed tensor is defined in a manner similar to Eq. 7:

$$A = \frac{2(H_1 - H_2)}{\mathrm{tr}(\boldsymbol{H})} \tag{9}$$

where H_1 and H_2 are the major and minor principal values, respectively, the boldface $\boldsymbol{H}$ refers to the mixed tensor, and $\mathrm{tr}(\boldsymbol{H}) = (H_1 + H_2)$ refers to the trace of $\boldsymbol{H}$. Mixed tensors for the strong and weak contacts of the granular assembly can also be defined in a manner similar to Eqs. 4, 5.

The definition of the mixed tensor was inspired by the microscopic definition of stress in a granular assembly, where the stress tensor is a volume average of the dyadic product between contact forces and branch vectors [5]. The orientations of contact forces are fairly similar to the orientations of contact normals (differences are constrained by the inter-particle friction), implying that the structural anisotropy captured by the mixed tensor is likely related to stress anisotropy. Figure 13 shows the orientational distribution of mixed tensor for (a) all contacts, (b) strong contacts, and (c) weak contacts.

5.4 Discussion of correlations between V_S anisotropy and fabric

An inspection of Figs 11, 12, 13 makes it apparent that assembly 1 and assembly 2 show different trends. Assembly 1 that has a stress history of simple shear has the entire network, including the subsets of strong and weak contacts aligned fairly uniformly, regardless of the type of fabric measure. The uniformity is more intense for contact and mixed tensors which incorporate information about
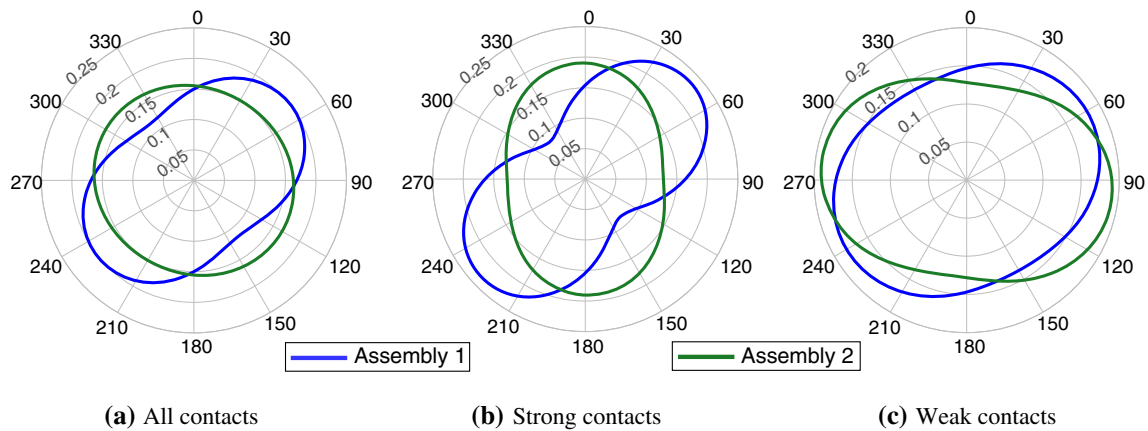
Fig. 12 Orientational distribution of branch tensor. The directions are clockwise from vertical (in degrees). **a** Assembly 1: $A = 0.26$, $\theta_1 = 52°$; Assembly 2: $A = 0.05$, $\theta_1 = -61°$. **b** Assembly 1: $A = 0.47$, $\theta_1 = 47°$; Assembly 2: $A = 0.20$, $\theta_1 = -3°$. **c** Assembly 1: $A = 0.14$, $\theta_1 = 62°$; Assembly 2: $A = 0.20$, $\theta_1 = -82°$
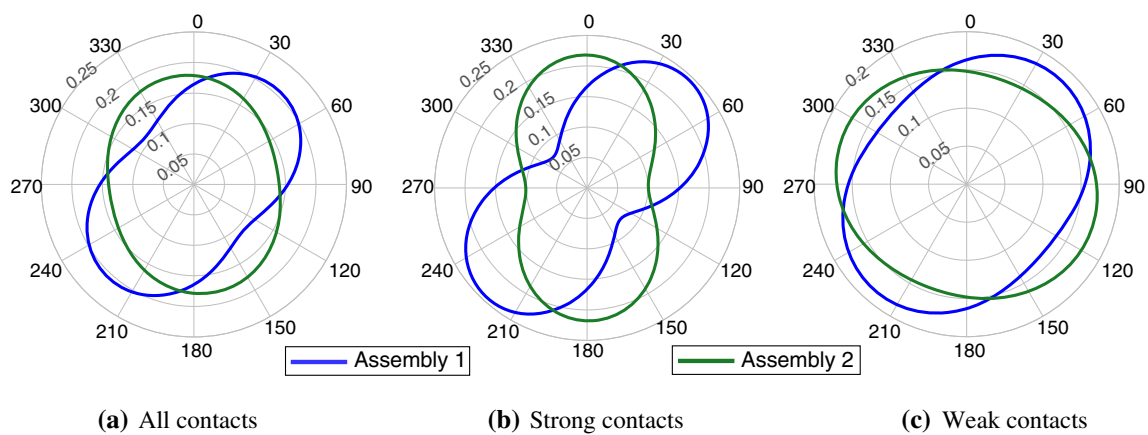
Fig. 13 Orientational distribution of mixed tensor. The directions are clockwise from vertical (in degrees). **a** Assembly 1: $A = 0.30$, $\theta_1 = 42°$; Assembly 2: $A = 0.13$, $\theta_1 = -11°$. **b** Assembly 1: $A = 0.53$, $\theta_1 = 43°$; Assembly 2: $A = 0.37$, $\theta_1 = -1°$. **c** Assembly 1: $A = 0.16$, $\theta_1 = 40°$; Assembly 2: $A = 0.09$, $\theta_1 = -69°$

contact normals. This is expected following the work by Estrada et al. [7], where it was shown that in the presence of rolling resistance—as is the case with non-spherical particles—simple shear stress history causes weak contacts to have the same alignment as strong contacts. This implies a high shear stiffness and a high V_S in the same direction, which is consistent with the results of V_S anisotropy in Fig. 10. This suggests that for a stress history of simple shear, V_S anisotropy is an effective indicator of fabric as well as liquefaction resistance. Note that the uniformity of orientation for the branch tensor is less intense since branch vectors are not collinear with contact normals. Nevertheless, it is clear that using branch vectors to quantify fabric does not provide additional insight for a stress history of simple shear.

Assembly 2, however, has a stress history of biaxial loading and shows a tendency to have its weak network aligned distinctly from the alignment of the strong network. This behavior under a stress history of biaxial loading was discussed by Radjai et al. [29] wherein the strong network is load-bearing and carries the bulk of the deviatoric load, while the weak network serves to support the strong network like an interstitial fluid. In our case, this behavior is most conspicuous in the anisotropic distributions of branch tensor and mixed tensor. The strong network has a predominantly vertical alignment, which is reflected in (1) a high V_S in the vertical direction, and (2) stable behavior under constant-volume vertical compression (Figs. 4 and 10). A high V_S in two other directions—along the horizontal direction and along 60° counter-clockwise from the vertical—can be understood by looking at the

anisotropy of weak contacts, especially for the case of the mixed tensor. The weak network seems to be able to sustain small elastic strains, resulting in a high value of V_S in directions where the weak network is aligned. Most of the deviatoric load is still carried by the strong network, as was evidenced by the spontaneous strain-softening behavior of assembly 2 under constant-volume horizontal compression (Fig. 4). The ability of the weak network to sustain small elastic strains suggests that for a stress history of biaxial loading, V_S anisotropy is not an effective indicator of fabric and should not be used to evaluate liquefaction resistance.

It is interesting to note that a knowledge of fabric anisotropy can give us information about V_S anisotropy and liquefaction resistance for both assemblies. Furthermore, for a stress history of simple shear, V_S anisotropy seems to give information both about fabric and liquefaction resistance. This has useful implications for the geotechnical community that uses V_S to model liquefaction resistance [2, 11, 41]. As discussed in Sect. 2.2, the simple shear stress history can be conceptually compared to a seismic history. This suggests that for sites with liquefiable soil deposits, that is to say recent soil deposits with a seismic history, the use of V_S to model liquefaction resistance may be justified from a micro-mechanical perspective. Caution must be exercised if the stress history is analogous to biaxial loading, for which our results suggest that the oft-quoted criticism about V_S being a small-strain elastic parameter while liquefaction is a medium-to-large-strain phenomenon seems to hold true.

Finally, we observe that the explanation of trends in V_S anisotropy seems to be most effective when using the mixed tensor fabric measure. This observation about the efficacy of the mixed tensor to capture stiffness anisotropy is not surprising, given that Kuhn et al. [15] made similar observations.

Remark 3 The motivation behind the current work was to incorporate more physics into the fabric-V_S relationship that may eventually help in mapping laboratory results to field conditions. The state of the art accounts for the effect of fabric on V_S (or other elastic parameters) via empirical correlations between V_S and confining stress or void ratio, where the empirical constants are assumed to quantify soil structure or fabric (e.g., [1, 8, 25, 36, 42]). Such studies have proven to be very useful but the inherent empiricism in the correlations means that they tend to be very soil-specific and have a limited range of application. By showing parallels in trends between fabric anisotropy (especially using the mixed tensor formulation) and V_S anisotropy, the current work complements the aforementioned state of the art. It now motivates the development of the next generation of correlations that can be more physics-based. Such a future development could involve (1)

in situ measurements of V_S, and (2) experiments and 3D simulations over a range of confining stresses and void ratios. Different sample preparation techniques could be explored such that V_S anisotropy in the experiments (or simulations) matches the V_S anisotropy in the field. Concurrently, the experiments/simulations could be used to develop correlations between V_S and fabric, using fabric quantification approaches similar to the types presented in this work. Once correlations have been developed, knowledge of in situ V_S anisotropy (especially for liquefiable soils, i.e., soils that are recent deposits and have a stress history of simple shear) may help determine in situ fabric.

6 Summary and conclusions

Figure 4 shows that the two 3200 grain assemblies— that are similar macroscopically but different microscopically— behave differently under constant-volume biaxial compression, implying different liquefaction resistance. Figure 10 shows that the two assemblies yield distinct anisotropic estimates of V_S. The macroscopic state of the assemblies was characterized by the volumetric stress p, the deviatoric stress q, and the void ratio e. The microscopic state was characterized by the fabric, which was quantified using the contact tensor, the branch tensor, and the mixed tensor. Figure 13 shows the orientational distribution of the mixed tensor, which helps understand trends in V_S anisotropy. Our results suggest that for liquefiable soil deposits, that is to say recent Holocene-age deposits with negligible cementation and a seismic history, the use of V_S to model liquefaction resistance may be justified from a micro-mechanical perspective. Care needs to be taken that inferring fabric and liquefaction resistance from V_S be done only for liquefiable soils under the aforementioned conditions. If a soil deposit has significant cementation and has a stress history that cannot be approximated using simple shear loading, then V_S— which is a small-strain elastic property—may not be an adequate measure to quantify fabric and consequently liquefaction resistance—which is a medium- to large-strain phenomenon. From a practical viewpoint, the constraints placed on the soils are not a big concern since liquefaction assessments are generally done on soils that meet the aforementioned constraints and are liquefiable, thus also supporting the prevalent practice of using V_S-based liquefaction charts. Furthermore, for liquefiable soils, a knowledge of V_S anisotropy may give us knowledge of in situ fabric, enabling development of a more physical procedure to map laboratory or simulation results to field conditions.
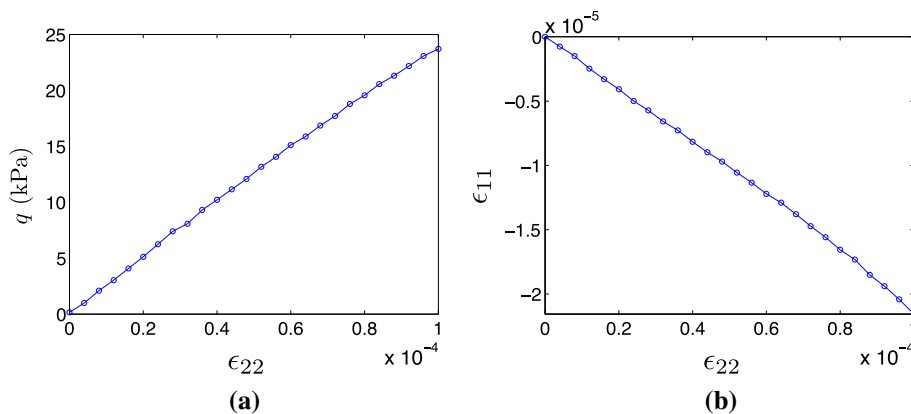
Fig. 14 Biaxial test at constant lateral stress for the 800 grain assembly, up to a set value of axial strain such that the response is linear. **a** deviator stress (q) versus axial strain (ϵ_{22}), yielding an elastic Young's modulus of 237 MPa. **b** Lateral strain (ϵ_{11}) vs axial strain (ϵ_{22}), yielding a Poisson's ratio of 0.21

Appendix

Verification exercise for numerical bender element test

In order to verify our implementation of the bender element test, we also estimate the shear wave velocity V_S by calculating G_{max} in a biaxial test. The two quantities are related as:

$$V_S = \sqrt{\frac{G_{max}}{\rho}} \tag{10}$$

where ρ is the density of the granular assembly. To measure G_{max}, an assembly in an isotropic stress state can be subjected to infinitesimal strains such that the response is linear or elastic. In our 3200 grain assembly, isotropic consolidation also results in shear stresses on the walls, typically of the order of about 1% of the confining pressure. Such a small amount of shear stress turned out to be sufficient to generate non-linear stress–strain curves, disabling the approximation of elastic constants. Hence, we resort to the smaller 800 grain assembly, prepared as described in Sect. 2.2. When the smaller assembly is consolidated to a pressure of 50 kPa, shear stresses on the wall are negligible ($\sim 0.2\%$ of confining pressure). Vertical loading to infinitesimal strains yields a linear stress–strain curve (Fig. 14), making it suitable for computing G_{max}, and consequently V_S, enabling a comparison with the V_S estimate obtained in Fig. 6.

Following the approach by O'Donovan et al. [27], we conduct a biaxial stress at constant horizontal stress, till a set value of vertical strain is achieved. As shown in Fig. 14, the plot of deviator stress q versus vertical strain ϵ_{22} is a straight line. The slope of the plot yields the elastic Young's modulus E:

$$E = \frac{dq}{d\epsilon_{22}} = 237 \text{ MPa} \tag{11}$$

where dq is the increment in deviatoric stress, and $d\epsilon_{22}$ is the increment in vertical strain. Note that deviatoric stress $q = \sigma_{22} - \sigma_{11}$. Furthermore, by monitoring the horizontal strain ϵ_{11}, we also obtain the Poisson's ratio v, as shown in Fig. 14:

$$v = \frac{-d\epsilon_{11}}{d\epsilon_{22}} = 0.21 \tag{12}$$

where $d\epsilon_{11}$ is the increment in horizontal strain. G_{max} is then calculated as:

$$G_{max} = \frac{E}{2(1+v)} = 97.9 \text{ MPa} \tag{13}$$

To obtain V_S, we need the density ρ of the granular assembly, which is calculated as:

$$\rho = \frac{\rho_{grains} \times A_{grains}}{A_{tot}} = 2.33 \times 10^3 \text{ kg/m}^3 \tag{14}$$

where $\rho_{grains} = 2.7 \times 10^3 \text{kg/m}^3$ is the density of grains as specified in Table 1, $A_{grains} = 4.3 \times 10^3 \text{ mm}^2$ is the total area of grains in the assembly, and $A_{tot} = 4.99 \times 10^3 \text{ mm}^2$ is the total area of the assembly. Finally using Eq. 10, the shear velocity is found to be $V_S = 205$ m/s, which is in good agreement with the V_S estimate obtained in Sect. 4.1.

References

1. Agnolin I, Roux JN (2007) Internal states of model isotropic granular packings. III. Elastic properties. Phys Rev E 76(6):061304
2. Andrus RD, Stokoe II KH (2000) Liquefaction resistance of soils from shear-wave velocity. J Geotech Geoenviron Eng 126(11):1015–1025

3. Azéma E, Radjai F, Saussine G (2009) Quasistatic rheology, force transmission and fabric properties of a packing of irregular polyhedral particles. Mech Mater 41(6):729–741

4. Cambou B, Jean M, Radjai F (2013) Micromechanics of granular materials. Wiley, New York

5. Christoffersen MM, Mehrabadi J, Nemat-Nasser S (1981) A micromechanical description of granular material behavior. J Appl Mech 48:339–344

6. Cundall PA, Strack ODL (1979) A discrete numerical model for granular assemblies. Géotechnique 29(1):47–65

7. Estrada N, Taboada A, Radjai F (2008) Shear strength and force transmission in granular media with rolling resistance. Phys Rev E 78(2):021301

8. Gu X, Hu J, Huang M (2017) Anisotropy of elasticity and fabric of granular soils. Granul Matter 19(2):33

9. Guo N, Zhao J (2013) The signature of shear-induced anisotropy in granular media. Comput Geotech 47:1–15

10. He X, Cai G, Zhao C, Sheng D (2017) On the stress-force-fabric equation in triaxial compressions: some insights into the triaxial strength. Comput Geotech 85:71–83

11. Idriss IM, Boulanger RW (2008) Soil liquefaction during earthquakes. Earthquake Engineering Research Institute, California

12. Jerves AX, Kawamoto RY, Andrade JE (2015) Effects of grain morphology on critical state: a computational analysis. Acta Geotechnica 1(3):257–275

13. Kanatani K-I (1984) Distribution of directional data and fabric tensors. Int J Eng Sci 22(2):149–164

14. Kawamoto R, Andò E, Viggiani G, Andrade JE (2016) Level set discrete element method for three-dimensional computations with triaxial case study. J Mech Phys Solids 91:1–13

15. Kuhn MR, Sun W, Wang Q (2015) Stress-induced anisotropy in granular materials: fabric, stiffness, and permeability. Acta Geotechnica 10(4):399–419

16. Ladd RS (1974) Specimen preparation and liquefaction of sands. J Geotech Geoenviron Eng 100(10):1180–1184

17. Ladd RS (1977) Specimen preparation and cyclic stability of sands. J Geotech Eng Div 103(6):535–547

18. Lee JS, Santamarina JC (2005) Bender elements: performance and signal interpretation. J Geotech Geoenviron Eng 131(9):1063–1070

19. Li X, Li X-S (2009) Micro–macro quantification of the internal structure of granular materials. J Eng Mech 135(7):641–656

20. Lim KW, Kawamoto RY, Andò E, Viggiani G, Andrade JE (2015) Multiscale characterization and modeling of granular materials through a computational mechanics avatar: a case study with experiment. Acta Geotechnica 91:1–13

21. Liu N, Mitchell JK (2006) Influence of nonplastic fines on shear wave velocity-based assessment of liquefaction. J Geotech Geoenviron Eng 132(8):1091–1097

22. Magoariec H, Danescu A, Cambou B (2008) Nonlocal orientational distribution of contact forces in granular samples containing elongated particles. Acta Geotechnica 3(1):49–60

23. Marketos G, O'Sullivan C (2013) A micromechanics-based analytical method for wave propagation through a granular material. Soil Dyn Earthq Eng 45:25–34

24. Mulilis JP, Arulanandan K, Mitchell JK, Chan CK, Seed HB (1977) Effects of sample preparation on sand liquefaction. J Geotech Eng Div 103(2):91–108

25. Ng TT, Petrakis E (1996) Small-strain response of random arrays of spheres using discrete element method. J Eng Mech 122(3):239–244

26. Nouguier-Lehon C, Vincens E, Cambou B (2005) Structural changes in granular materials: the case of irregular polygonal particles. Int J Solids Struct 42(24):6356–6375

27. O'Donovan J, O'Sullivan C, Marketos G (2012) Two-dimensional discrete element modelling of bender element tests on an idealised granular material. Granul Matter 14(6):733–747

28. O'Donovan J, O'Sullivan C, Marketos G, Wood DM (2015) Analysis of bender element test interpretation using the discrete element method. Granul Matter 17(2):197–216

29. Radjai F, Wolf DE, Jean M, Moreau J-J (1998) Bimodal character of stress transmission in granular packings. Phys Rev Lett 80(1):61

30. Rothenburg L, Kruyt NP (2004) Critical state and evolution of coordination number in simulated granular materials. Int J Solids Struct 41(21):5763–5774

31. Sanchez-Salinero I, Roesset JM, Stokoe KH II (1986) Analytical studies of body wave propagation and attenuation. Technical report, DTIC Document

32. Seed HB, Idriss IM, Makdisi F, Banerjee N (1975) Representation of irregular stress time histories by equivalent uniform stress series in liquefaction analyses. Technical Report EERC 75-29, Earthquake Engineering Research Center

33. Seed HB, Idriss IM (1971) Simplified procedure for evaluating soil liquefaction potential. Journal of Soil Mechanics & Foundations Div 97(9):1249–1273

34. Seed HB, Peacock WH (1971) Test procedures for measuring soil liquefaction characteristics. J Soil Mech Found Div 97(8):1099–1119

35. Shirley DJ, Hampton LD (1978) Shear-wave measurements in laboratory sediments. J Acoust Soc Am 63(2):607–613

36. Stokoe, KH, Lee, SHH, Knox, DP (1985) Shear moduli measurements under true triaxial stresses. In: Advances in the art of testing soils under cyclic conditions. ASCE, pp 166–185

37. Tu X, Andrade JE (2008) Criteria for static equilibrium in particulate mechanics computations. Int J Numer Methods Eng 75:1581–1606

38. Viggiani G, Atkinson JH (1995) Interpretation of bender element tests. Géotechnique 45(1):149–154

39. Vlahinić I, Andò E, Viggiani G, Andrade JE (2014) Towards a more accurate characterization of granular media: extracting quantitative descriptors from tomographic images. Granul Matter 16(1):9–21

40. Yamashita S, Kawaguchi T, Nakata Y, Mikami T, Fujiwara T, Shibuya S (2009) Interpretation of international parallel test on the measurement of g_{max} using bender elements. Soils Found 49(4):631–650

41. Youd TL, Idriss IM (2001) Liquefaction resistance of soils: summary report from the 1996 nceer and 1998 nceer/nsf workshops on evaluation of liquefaction resistance of soils. J Geotech Geoenviron Eng 127(4):297–313

42. Zeghal M, Tsigginos C (2015) A micromechanical analysis of the effect of fabric on low-strain stiffness of granular soils. Soil Dyn Earthq Eng 70:153–165

43. Zhao J, Guo N (2015) The interplay between anisotropy and strain localisation in granular soils: a multiscale insight. Gotechnique 65(8):642–656